Prepublished copy

Nature Environment & Pollution Technology

This is a peer-reviewed prepublished version of the paper to be published in Vol. 25, No. 4, December 2026 issue

Type of the Paper (Original Research, Review)

Eco-Friendly Degradation of Textile Azo Dye Reactive Orange ME2RL Using *Pseudomonas stutzeri*-mediated Iron oxide Nanoparticles

P. Zambare[1,2,4] A. Raut[2]† and S. Kanase[1,3]

[1]Rayat Institute of Research and Development, Satara, 415001, Maharashtra, India

[2]Department of Microbiology, Yashavantrao Chavan Institute of Science, Satara, 415001, Maharashtra, India

[3]Department of Microbiology, Yashwantrao Chavan College of Science, Karad, 415110, Maharashtra, India

[4]Department of Microbiology, Shivaji University, Kolhapur, 416004, Maharashtra, India

†Corresponding author: A. Raut; rautavinash@gmail.com

ORCID ID: 0000-0001-9609-3704

Key Words	*Pseudomonas stutzeri*, Reactive orange ME2RL, Iron oxide, Nanoparticles, Biophysical analysis
DOI	https://doi.org/10.46488/NEPT.2026.v25i04.B4422 (DOI will be active only after the final publication of the paper)
Citation for the Paper	Zambare, P., Raut, A. and Kanase, S., 2026. Eco-friendly degradation of textile azo dye reactive orange ME2RL using *Pseudomonas stutzeri*-mediated iron oxide nanoparticles. *Nature Environment and Pollution Technology*, 25(4), B4422. https://doi.org/10.46488/NEPT.2026.v25i04.B4422

Abstract: The discharge of synthetic azo dyes from textile industries poses serious environmental and health risks due to their genotoxic, mutagenic and carcinogenic nature. In present work, eco-friendly iron oxide (Fe_2O_3) nanoparticles were biosynthesized using *Pseudomonas stutzeri* with ferric chloride as a precursor under ambient conditions and applied for the degradation of the textile dye Reactive Orange ME2RL. The synthesized nanoparticles were characterized by UV–Visible spectroscopy, FTIR, SEM, EDX, HRTEM, and DLS, confirming the formation of stable nanoscale Fe_2O_3 particles. The nanoparticles exhibited efficient catalytic activity, achieving nearly 80% degradation of Reactive Orange ME2RL within 45 minutes. The degradation pathway and formation of intermediate metabolites were confirmed using UV–Visible spectroscopy, FTIR, HPLC, and GC–MS analyses. Furthermore, phytotoxicity and fish toxicity assays indicated reduced toxicity of the degradation products. The results demonstrate that biosynthesized Fe_2O_3 nanoparticles offer a rapid, efficient, and environmentally sustainable approach for the remediation of azo dye-contaminated textile wastewater.

Graphical abstract

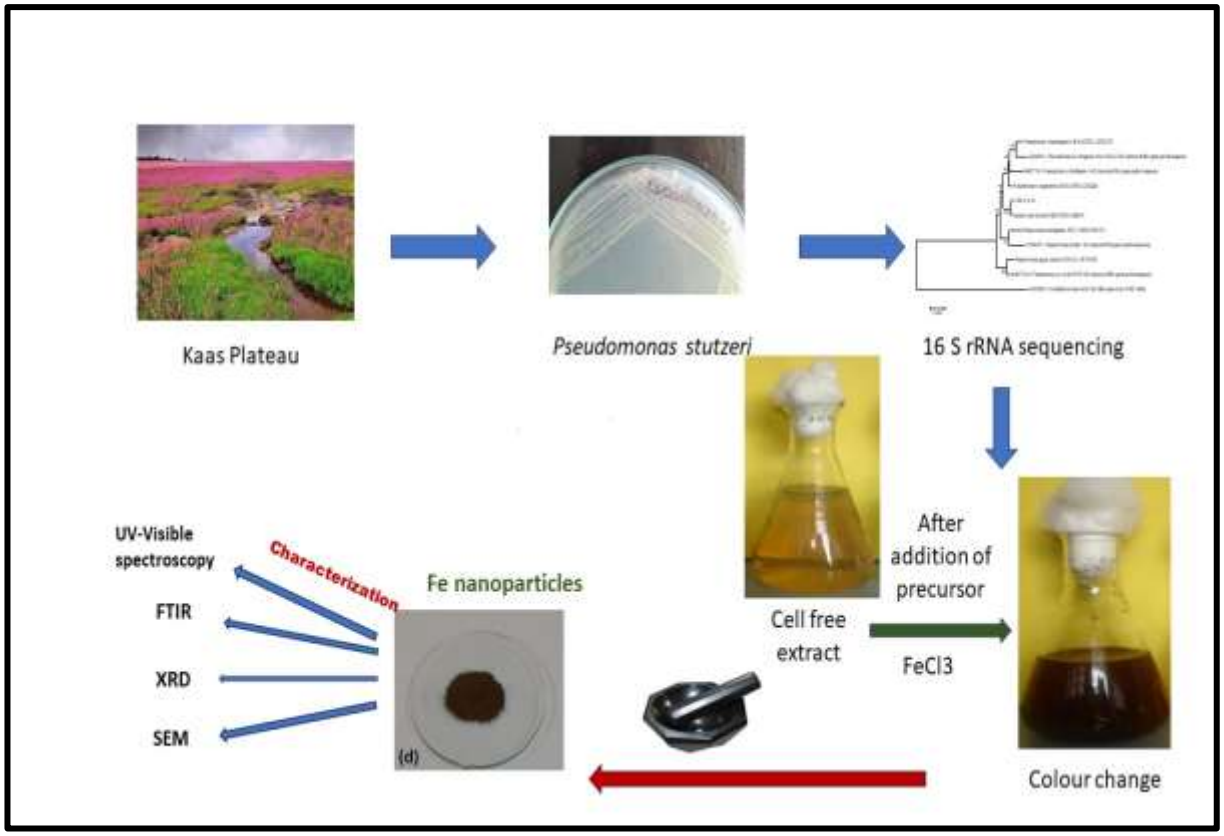

Biosynthesis of iron nanoparticles using bacteria

1. INTRODUCTION

Textile sectors secure a special position in the Indian economy by boosting industrial production, exports, and employment (Chavan 2001). However, because it includes the use of synthetic dyes that have a negative impact on the environment and life forms, the effluent produced from the textile industry has turned into a constant source of environmental pollution (Banat et al. 1997). Textile wastewater is typically characterized by intense color, high chemical oxygen demand (COD), total dissolved solids (TDS), and the presence of recalcitrant aromatic structures, making conventional treatment highly challenging. The persistence of these dyes in aquatic ecosystems leads to reduced light penetration, inhibition of photosynthesis, and long-term ecological imbalance (Patel & Bhatt 2022; Haroon, K.et al. 2023).

Scientists are captivated by metal nanoparticles because of their remarkable chemical, electrical, and optical properties. Green synthesis of such nanoparticles is simple, ecologically sound, and offers a quick means to meet the growing need for safe, non-toxic, and biocompatible nanoparticles around the world (Khan et al. 2019). Researchers have taken a particular interest in green synthesis of nanoparticles utilizing microbes due to simple handling processes, environmentally friendly disposal, and significantly simpler downstream processing (Annamalai et al. 2021). Among all microbes, bacteria have the innate capacity to reduce a given metal to produce metal nanoparticles (Srivastava &Constanti 2012). Microbial synthesis not only avoids toxic reducing agents used in chemical methods but also enables precise control over nanoparticle morphology through enzymatic and metabolic pathways. This makes microbial nanotechnology a rapidly emerging tool for sustainable environmental remediation (Annamalai et al. 2021).

Due to their genetic diversity and adaptable metabolic systems, microbes are a preferable choice for the biological remediation of dye pollution (Banat et al. 1997; Shakoor, S. et al. 2025). Additionally, biological treatment uses fewer reagents and produces less sludge than many physicochemical methods, making it a more affordable and eco-friendly option. It can result in the total mineralization of dyes and is also cost-effective (Pandey et al. 2007). There is great hope that iron nanoparticles (FeNPs) can help reduce pollution in the environment.

The phylum *Proteobacteria* includes *Pseudomonas stutzeri*, which is classified as group I of Palleroni's DNA–rRNA homology group (Palleroni et al. 1973; Palleroni 1984). It is currently acknowledged to be a member of the *Gammaproteobacteria* class. *P. stutzeri* is a widely distributed nonfluorescent denitrifying bacterium that has also been identified in humans as an opportunistic pathogen (Rossello et al. 1991). The taxonomy of such varied taxonomic groups has been clarified over the past decades, and the unique metabolic properties of this species have garnered a lot of attention. Some strains of this organism are able to fix dinitrogen, and it has served as a reference organism for studies on denitrification; other strains break down contaminants or interact with toxic metals, and several strains also show natural transformation capabilities, which makes them important for studying environmental gene transfer (Palleroni et al. 1970). Importantly, P. stutzeri has been reported to tolerate and transform diverse xenobiotics, making it a promising candidate for bio-nanotechnological applications, including microbial nanoparticle synthesis and dye biodegradation (Shahriarinour et al. 2021).

Textile, culinary, leather, cosmetic, plastic, and paper sectors currently use a plethora of organic dyes for aesthetic purposes, many of which may be hazardous and constitute a serious threat to the environment (Forgacs et al. 2004).

One of the difficult issues facing environmentalists and industry is treating and removing organic dyes from textile effluent. There are several physicochemical techniques already in use; however, these are often inefficient and may produce new chemicals that require additional treatments. Techniques such as ozonation, coagulation–flocculation, adsorption, and membrane filtration may achieve partial color removal but often fail to degrade dye molecules completely, generating secondary pollution and incurring high operational costs (Periyasamy 2024).

In recent years, there has been a significant increase in interest in advanced technologies that use nanocatalysts to eliminate dyes and other organic pollutants from the environment (Naz et al. 2021). A simple and sustainable method that does not require organic solvents is to treat dyes in the presence of a biocompatible, environmentally safe catalyst. Reactive Orange Me2RL is a di-azo dye that is essential to the textile industry and is commonly used for coloring wool, silk, leather, paper, and polyamide fibre. Over the past few years, the degradation of this dye has gained considerable attention. This dye's complex aromatic backbone and multiple azo linkages render it resistant to traditional biological degradation, highlighting the need for integrated nano-biotechnological approaches for efficient treatment (Joshi et al. 2015).

In this study, the bacterium *Pseudomonas stutzeri*, known for degrading di-azo dyes containing two –N=N– azo bonds (Joshi et al. 2020), was evaluated for its efficiency in bioremediation and degradation processes. In this context, efforts were made to study the biodegradation of a common textile di-azo dye, Reactive Orange Me2RL, using iron nanoparticles synthesized by an isolated strain of *Pseudomonas stutzeri* (present study). The combined application of microbially synthesized FeNPs and dye-degrading bacteria provides a synergistic strategy capable of enhancing both catalytic efficiency and biodegradation, aiming toward a sustainable, cost-effective, and eco-friendly treatment method for textile effluents.In present study, we focused on degradation of Orange ME2RL textile dye using Fe_2O_3 nanoparticles synthesized using *Psedomonasstutzeri*.Orange ME2RL damages the eyes, mucous membranes, and upper respiratory tract in addition to being known to cause cancer (Gupta et al 2006). By blocking light and oxygen from entering water bodies, it is also known to raise biological oxygen demand, which has an impact on marine life. As a result, both of these colors should basically be eliminated from wastewater before being released into water bodies since they are known to be harmful to man and may have long-lasting impacts .(Ali H.2010)

2. MATERIALS AND METHODS

2.1 Materials:

The nutritional agar, 99% pure $FeCl_3$, and nutrient broth used in this investigation were all procured from Himedia Laboratories Pvt. Ltd., an Indian company. Materials were procured from Sigma Aldrich in India and included Reactive Orange ME2RL, ethyl acetate, $FeCl_3$, and methanol. All components were derived from analytical reagent-grade chemicals.

2.2 Methods:

2.2.1 Iron nanoparticle biosynthesis

The bacterial strain *Pseudomonas stutzeri* was isolated from a soil sample of Kaaspathar at Satara, Maharashtra, India. Molecular identification of the isolated strain was performed by 16S rRNA sequencing at NCMR, Pune (Mukherjee & Dutta 2019). The pure culture of *Pseudomonas stutzeri* was inoculated into sterile nutrient broth and incubated at 28 °C for 24 hours with shaking at 120 rpm. After harvesting and washing the bacterial biomass, it was suspended in sterile distilled water and agitated at 120 rpm for 24 hours at 28 °C. The cell-free extract (CFE) obtained after centrifugation was used for nanoparticle synthesis.

To initiate nanoparticle formation, 1 mM $FeCl_3$ was added to the CFE in equal volume, and the mixture was stirred at 120 rpm at 28 °C. A 1 mM $FeCl_3$ solution without CFE served as the control. The development of iron nanoparticles was monitored visually and through UV–visible spectroscopy at regular intervals. The ability of the isolated *P. stutzeri* to synthesize iron nanoparticles was further supported by earlier reports of microbial nanoparticle production by *Pseudomonas* spp. (Vasantharaj et al. 2019).

2.2.3 Characterization of Iron Nanoparticles

The excitation spectra of biosynthesized iron nanoparticles were recorded using a UV–Visible spectrophotometer (Systronics AU-270I) operating in the wavelength range of 400–800 nm (Velusamy et al. 2016). Crystallinity was determined using X-ray diffraction (XRD; Bruker D8 Advance) (Giuli et al. 2015). XRD analysis was performed in the 2θ range of 20°–80° at 40 kV and 40 mA. XRD is widely used to identify crystal structure and nanoparticle phase composition (Holzwarth & Gibson 2011).Scanning electron microscopy (SEM) was used to examine the morphology of iron nanoparticles. High-resolution transmission electron microscopy (HRTEM) with an FEI Tecnai G2 U-Twin instrument was used to determine particle size and shape. Dynamic light scattering (DLS) analysis was performed using a Nicomp 388 ZLS system to determine hydrodynamic size distribution (Chicea et al. 2012).Fourier transform infrared (FTIR) spectroscopy (Shimadzu FTIR-8400) covering 400–4000 cm^{-1} was performed to identify biomolecules involved in nanoparticle reduction and stabilization (Zhao et al. 2016; Carabante et al. 2009).

2.2.4 Degradation of Reactive Orange Me2RL Using Iron Nanoparticles

The catalytic degradation potential of biosynthesized iron nanoparticles was evaluated using Reactive Orange Me2RL dye. A 1 mM concentration of FeNPs was added to 100 mL of dye solution (1 mg/100 mL), and

the mixture was agitated at 120 rpm for 30 min (Al-Musawi et al. 2022).At fixed intervals, 2 mL aliquots were withdrawn and the absorbance at 494 nm was measured to calculate degradation percentage using Equation 1:

$$\text{Degradation (\%)} = \frac{D_0 - D_1}{D_0} \times 100 \quad \text{.....(1)}$$

Where,

D_0 = initial absorbance

D_1 = final absorbance

2.3 Study of Metabolites of the Degraded Dye

2.3.1 UV–Visible Spectroscopy

The spectral changes of control and treated dye samples (400–800 nm) were analyzed to confirm biodegradation rather than superficial decolorization (Wu et al. 2022).

2.3.2 Fourier Transform Infrared Spectroscopy (FTIR)

FTIR analysis was performed to understand functional group alterations during degradation and nanoparticle interaction (Katata-Seru et al. 2018).

2.3.3 High-Performance Liquid Chromatography (HPLC)

HPLC analysis was performed using a C18 column (4.6 × 250 mm) with methanol as mobile phase at 1 mL/min. A UV detector was used to analyze dye metabolites at maximum absorption wavelengths (Ferreira et al. 2020).Supernatants from degradation experiments (0–45 min) were analyzed, and metabolites were extracted using ethyl acetate, dried with anhydrous Na_2SO_4, evaporated, and reconstituted in HPLC-grade methanol (Apine et al. 2023).

2.3.4 Gas Chromatography–Mass Spectrometry (GC–MS)

Extracted metabolites were subjected to GC–MS analysis after solvent evaporation and reconstitution. This process followed standard extraction protocols for dye degradation metabolites (Castro et al. 2020).

2.3.5 Antibacterial Activity of Iron Nanoparticles

Antibacterial properties of FeNPs were examined using the agar well diffusion method. Test organisms included *Proteus vulgaris* (NCIM-2813), *Salmonella typhimurium* (NCIM-2501), *Staphylococcus aureus* (NCIM-2654), and *Pseudomonas aeruginosa* (NCIM-5032). Antibiotic solutions, FeNPs, and combinations were loaded into agar wells and incubated at 37 °C for 24 hours. Zones of inhibition were measured (mm), and percent fold-increase in antibacterial activity was calculated by Equation 2: (Mane et al. 2008).

Percent Fold Increase $= \frac{B-A}{A}$.....(2)

Where

A = inhibition zone of antibiotic

B = inhibition zone of antibiotic + FeNPs

2.4 Phytotoxicity Studies

Phytotoxicity of the parent dye and its degradation metabolites was assessed on four agricultural seed types: *Vigna radiata* (green gram), *Triticum aestivum*, *Vigna unguiculata*, and *Pisum sativum*. Seeds were treated with up to 400 ppm of dye and metabolite solutions (Aly et al. 2023). Distilled water served as control. Parameters measured after 7 days included germination percentage and plumule/radicle length (Ameur et al. 2012).

2.5 Fish Toxicity Studies

Glass aquaria were sterilized using 0.1% potassium permanganate to prevent fungal contamination (Hanafi & Sapawe 2020). Fish were acclimatized and then exposed to varying concentrations of Reactive Orange Me2RL dye. LC_{50} values were determined after 96 hours of exposure. Histological analysis of treated fish was conducted to assess tissue alterations (Islam et al. 2021).

2.6 Determination of LC_{50} and Percent Mortality

A simple approach for determining a substance's toxicity is LC_{50}. The stock's well-acclimated fish were split up into six batches, each with ten robust fish to represent each pesticide. After that, they were moved to glass aquariums with varying dye concentrations (1.25, 2.5, 3.75, 5.00, 6.25 , 7.5 , 8.75ppm). The fish were subjected to the corresponding concentration for a predetermined amount of time, and the mortality was tracked for 96 h for each concentration. For every concentration of dye, the quantity of dead fish was counted after 24, 48, 72, and 96 h. To confirm the mortality rate and the LC_{50} value, the trials were conducted three times (Islam et al. 2021). Determination of percent mortality using the following formula 3:

$$\% \text{ Mortality} = \frac{\text{Number of dead fish}}{\text{Initial number of stocked fish}} \times 100 \text{.....(3)}$$

3. RESULTS AND DISCUSSION

3.1. Overview

In the current investigation,bacterial strain *Pseudomonas stutzeri* was used for the biosynthesis of iron nanoparticles. The catalytic efficiency of these biosynthesized nanoparticles toward Reactive Orange Me2RL degradation was found to be remarkable. This rapid degradation highlighted the superior reactivity and surface

characteristics imparted by the green synthesis route. Instrumental analysis further confirmed the conversion of the parent azo dye into less complex, non-toxic metabolites, validating the complete breakdown of chromophoric groups. Apart from dye degradation, the biosynthesized nanoparticles also showed excellent antibacterial activity against pathogenic bacterial strains. Moreover, an additive effect was also observed when combined with conventional antibiotics. Importantly, phytotoxicity and fish toxicity assays revealed that the degraded dye products were non-toxic, reinforcing the environmental compatibility of the degradation process. Overall, the integrated characterization, catalytic activity, and toxicity studies collectively demonstrate the potential of *Pseudomonas stutzeri* derived iron nanoparticles as an efficient, eco-friendly approach for textile dye bioremediation.

3.1.1. Biosynthesis of Iron Nanoparticles

The biosynthesis of iron nanoparticles (Fe NPs) using isolated *Pseudomonas stutzeri*was confirmed by visual changes that occurred during the bioreduction of ferric ions.

Fig. 1:A) Cell-free extract, B) Colour change after addition of precursor ($FeCl_3$) solution

Upon addition of $FeCl_3$ solution to CFE, the reaction mixture showed a gradual colour change from pale yellow to a characteristic reddish-brown within 24 h, intensifying further over the next 48 h (Fig. 1). This color change was due to the NADH-dependent reductases that initiated this redox process, while proteins and polysaccharides simultaneously act as capping agents, binding to nanoparticle surfaces through functional groups such as amide, hydroxyl, and carboxyl (Acharya et al. 2025). This chromatic shift is a well-established indicator of nanoparticle formation and was attributed to the excitation of surface plasmon resonance (SPR), arising when iron nuclei begin nucleating and accumulating into nanoscale clusters (Jana, Ganguly& Pal 2016).

3.2. Characterization of Nanoparticles

3.2.1. UV Visible Spectroscopy

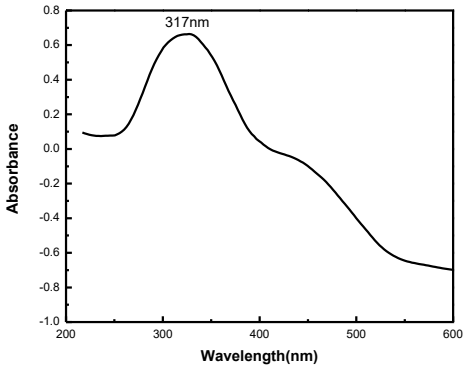

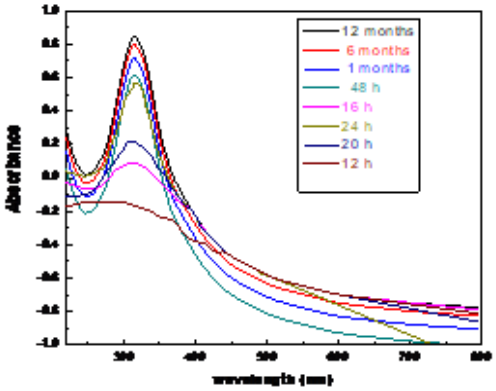

Fig. 2: UV spectrum of iron nanoparticles synthesized by *Pseudomonas stutzeri*

Apart from visual confirmation, the biosynthesis of the nanoparticles was further confirmed using UV spectroscopy which provided a sensitive indication of nucleation and growth dynamics in metal nanostructures. It was observed that the initial CFE exhibited no significant absorbance in the visible range, which confirmed the absence of pre-existing nanoparticles. The addition of $FeCl_3$ showed the distinct absorption band at 317 nm, corresponding to the characteristic SPR of biogenic iron nanoparticles (Fig. 2).The gradual development and intensification of this peak over time reflected the continuous reduction of Fe^{3+} ions and the subsequent growth of Fe^0 nuclei into stable nanoparticles. The appearance of the 317 nm peak is consistent with earlier reports on microbial and phytogenic iron nanoparticles, indicating successful synthesis under ambient conditions (Nurbas, Ghorbanpoor&Avci 2017). Variations in peak sharpness and intensity provide mechanistic insights: the moderate bandwidth suggests a relatively narrow size distribution, aligning with TEM and DLS findings. The stability of the absorbance peak without significant red-shifting further implies controlled growth and effective capping by biomolecules present in the CFE, which restrict particle aggregation. Overall, UV–visible analysis not only confirms nanoparticle formation but also reveals the kinetics and stabilization behaviour associated with biogenic synthesis, demonstrating the efficiency of *P. stutzeri*-mediated Fe NP production.

The stability of the synthesized Fe_2O_3 nanoparticles was evaluated by monitoring their UV–visible absorption spectra over an extended storage period ranging from 12 h to 12 months (Fig. X). The spectra exhibit a characteristic absorption band in the visible region around ~420–450 nm, which is associated with the electronic transitions of iron oxide nanoparticles. No significant shift in the absorption maximum or drastic change in spectral shape was observed during the monitoring period. The overall preservation of the spectral profile indicates that the Fe_2O_3 nanoparticles remain structurally and optically stable for up to 12 months under storage conditions, suggesting good colloidal stability.

3.2.2. FTIR

FTIR measurements of iron nanoparticles helped to reveal information about chemical changes in functional groups complex in the reduction process of iron ions to iron nanoparticles (Giuli et al. 2015).

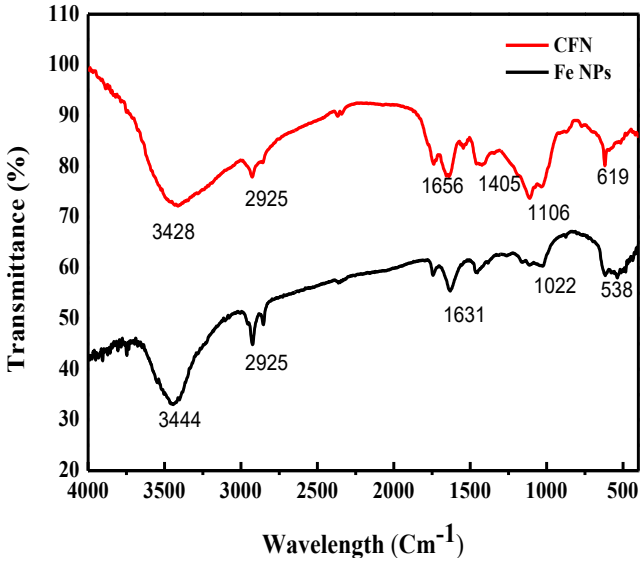

Fig. 3:FTIR of iron nanoparticles

Fig. 3 showed four distinct peaks at 3344 cm^{-1}, 2925 cm^{-1}, 1631 cm^{-1}, 1022 cm^{-1}, and 538 cm^{-1}, indicating FeNPs. The asymmetric stretching of C–H bonds, C–O stretching, and O–H stretching vibrations (alcoholic or phenolic) are all accompanied by these peaks. This shows that functional groups significantly aid in the stabilization and capping of iron nanoparticle production. A new peak at 538 cm^{-1} in FeNPs confirms the formation of Fe–O bonds, indicating successful synthesis and capping by biomolecules.

3.2.3. XRD

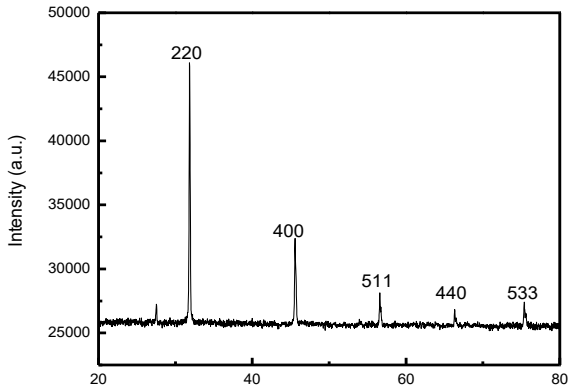

Fig. 4: XRD pattern of iron nanoparticles

To further understand the formation and crystallinity of synthesized iron nanoparticles, XRD examination was conducted (Holzwarth& Gibson 2011). XRD pattern, shown in Fig. 4, reveals distinct diffraction peaks at 31.94°, 45.5°, 56.6°, 66.33°, and 75.38°, corresponding to hill plane values of 220, 400, 511, 440, and 533 respectively, which match the JCPDS card 19-0629. The crystalline structure and phase of iron nanoparticles are explained by the strong diffraction peak, which indicates the synthesis of Fe_3O_4 nanoparticles. Nanoparticle size estimated via the Debye–Scherrer equation is 32 nm, indicating a large surface area–to–volume ratio. The size of a nanoparticle's crystallite is determined using the Debye–Scherrer formula (Chicea, Indrea&Cretu 2012).

3.2.4. DLS

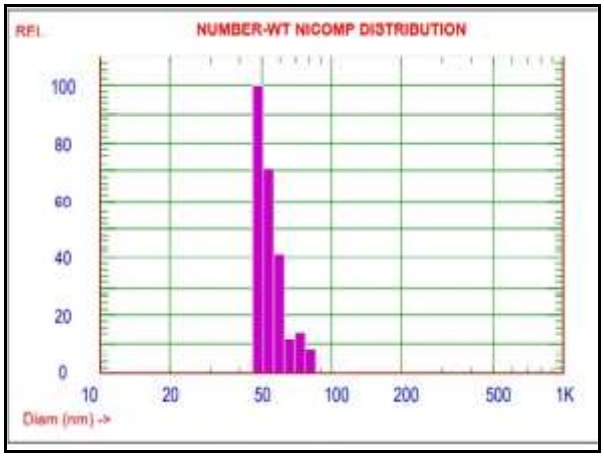

Fig. 5: Hydrodynamic particle size measurement using the DLS (volume-weighted) method

DLS method was used to analyse the nanoparticle size distribution profile (Javidparvar, Ramezanzadeh & Ghasemi 2016). Particle size distribution revealed the sample's hydrodynamic particle size. The majority of the particles were between 50 nm and 100 nm, with a 50 nm average particle size (Fig. 5). Hydrodynamic size closely resembles the particle size determined by SEM analysis, even though this method frequently yields larger nanoparticles due to agglomeration. The DLS particle size study showed iron nanoparticles sized 50–100 nm. The hydrodynamic size includes both the metallic core and the coating material. DLS measures the hydrodynamic

diameter of nanoparticles dispersed in a liquid medium. This includes not only the nanoparticle core but also the surrounding solvation layer, surface-bound biomolecules, and possible agglomeration in the suspension. As a result, the measured particle size appears larger. (Bhattacharjee 2016)

3.2.5. SEM

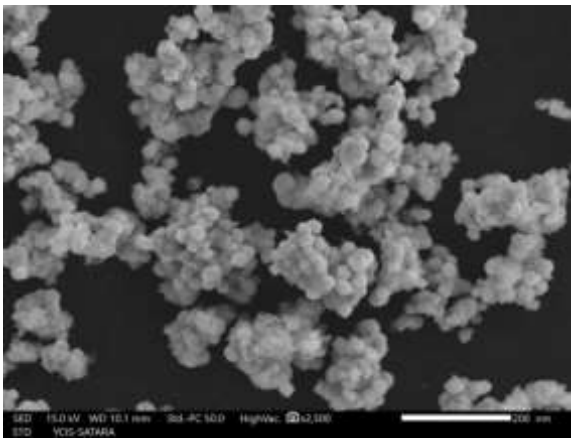

Fig. 6:SEM images of iron nanoparticles

Surface morphology of iron nanoparticles was analyzed by SEM (Saha&Bhunia 2020) as shown in Fig. 6. Monodispersed FeNPs of size 20–50 nm were visualized from the SEM micrograph. The particles appeared smooth and highly crystalline. Micrographic illustrations showed with distinct borders, with an average size of 33 nm.

3.2.6. HRTEM

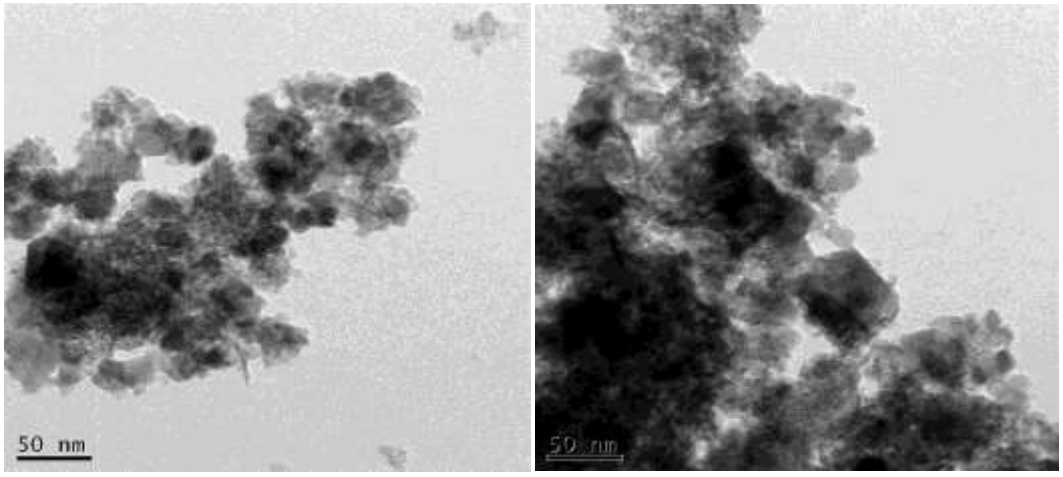

Fig. 7: HRTEM images of an iron nanoparticle

The size and morphology of optimized nanoparticles were observed by HRTEM, which confirmed the formation of almost spherical iron nanoparticles (Fig. 7). The size of iron nanoparticles is approximately 20–50 nm. Similar findings were reported in previous studies (Katata-Seru et al. 2018; Sekar et al. 2012).

3.3. Catalytic Degradation of Reactive Orange Me2RL Using Biogenic Iron Nanoparticles

Fig. 8: Gradual colour changes from orange to colourless after the addition of iron

Captivatingly, upon addition of iron nanoparticles into the dye solution (1 mg/100 mL), gradual degradation occurred in visible light. Colour of solution changed from orange to colourless within 45 minutes (Fig. 8). Outcomes are consistent with earlier reports (Joshi et al. 2015).

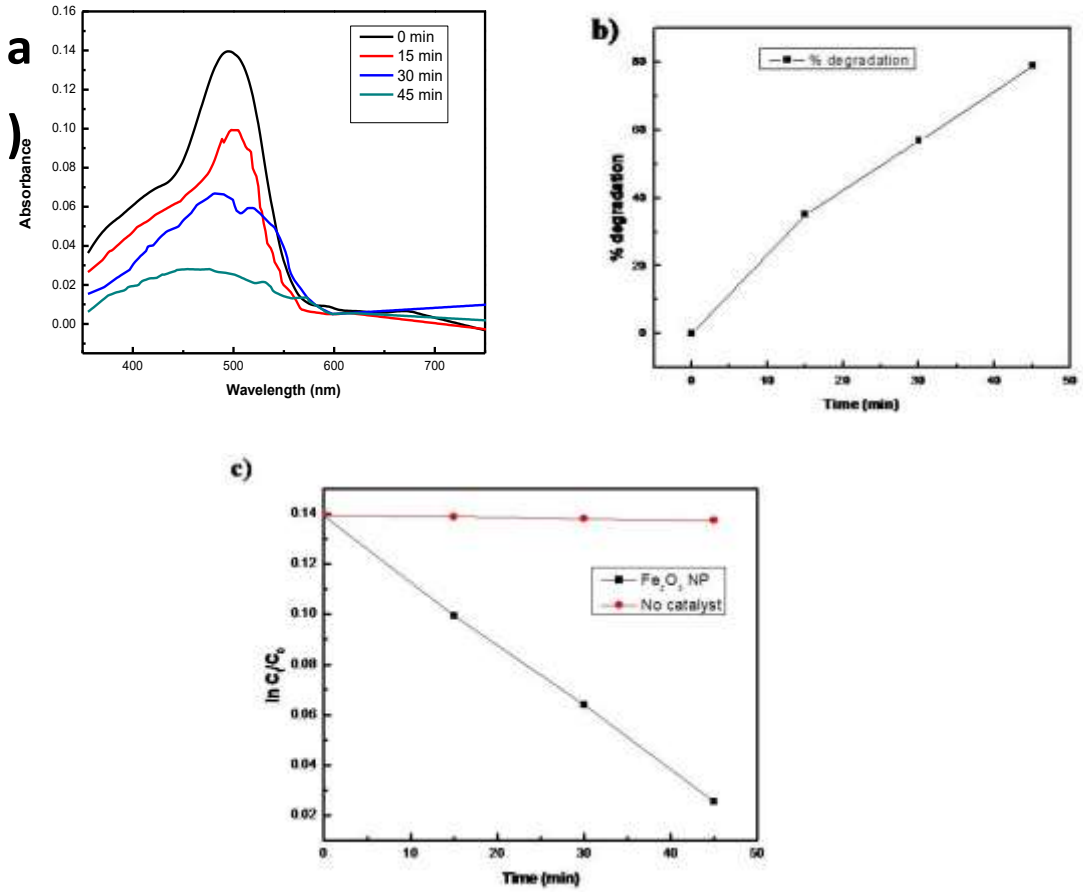

Fig 9.(a) UV–Visible Absorption spectra of Orange ME2RL dye using Fe_2O_3 nanoparticles various time interval, (b)- Degradation % of Orange ME2RL dye with time inpresence of Fe_2O_3 nano material, (c)- ln(Ct/Co) verses degradation time plot for finding the reaction rate constant (kapp).

The distinguishing absorption peak at 494 nm was monitored to investigate the catalytic activity of iron nanoparticles. The reduction reaction was characterized by a steady decline in the maximum intensity (kmax) at 494 nm with little shift in λmax. The peak at 494 nm decreased within 45 minutes, suggesting that Reactive Orange Me2RL was degrading (Fig. 9). Small peaks and a broad band at 600–750 nm suggest intermediate by-products (Forgacs, Cserháti & Oros 2004).

The degradation experiments were performed under ambient laboratory light conditions, and therefore the observed dye removal may involve photocatalytic activity of Fe_2O_3 nanoparticles.The generation of highly reactive hydroxyl radicals (•OH) during the photodegradation process is initiated by the formation of electron–hole (e^-/h^+) pairs on the surface of photoactivated catalysts. **Fig. 9 (d)** illustrates a simplified mechanism describing the formation of free radicals (•OH) and the photocatalytic degradation of Orange ME2RL dye. Upon light irradiation, electrons are excited from the valence band to the conduction band, resulting in the generation of electron–hole pairs (e^-/h^+) (Eq. (4)). The photogenerated electrons in the conduction band can migrate to the hematite surface and reduce Fe^{3+} ions (Eq. (5)). These electrons may also interact with hydrogen peroxide molecules, producing reactive radical species (Eq. (6)). Meanwhile, the photogenerated holes react with surface-adsorbed water molecules (Eq. (7)) as well as with HO^- by-products (Eq. (8)). In addition, surface Fe^{2+} can be oxidized to Fe^{3+} in the presence of adsorbed H_2O_2 (Eq. (9)), which further enhances the production of •OH radicals that serve as the primary oxidizing species responsible for dye degradation [Vu et al., 2019., Huang et al 2015].

$Fe_2O_3 + hv \rightarrow e^- + h^+$ (4)

$Fe_2O_3 + e^- \rightarrow Fe^{2+}$ (5)

$e^- + H_2O_2 \rightarrow \bullet OH + HO^-$ (6)

$h^+ + H_2O \rightarrow H^+ + \bullet OH$ (7)

$HO^- + h^+ \rightarrow \bullet OH + H^+$ (8)

$Fe^{2+} + H_2O_2 \rightarrow Fe^{3+} + \bullet OH + HO^-$ (9)

Additionally, it is important to consider that •OH radicals can be formed by direct photolysis as follows:

$H_2O_2 + hv \rightarrow 2\ \bullet OH$ (10)

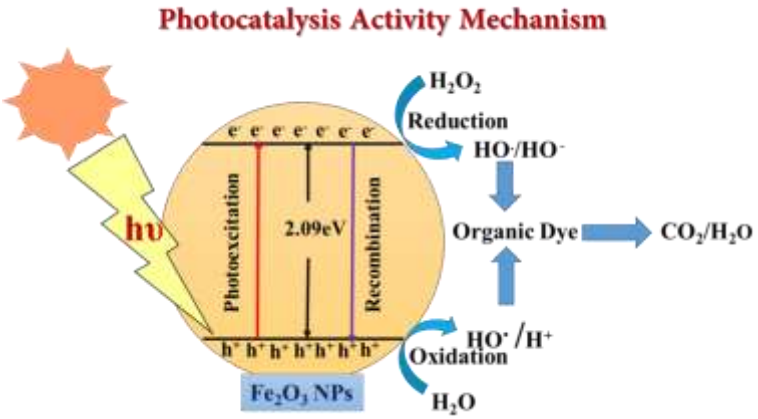

Fig. 10 (d): Photodegradation mechanism of Orange ME2RL dye in the presence of Fe_2O_3 nanoparticles.

The degradation experiments were conducted at an initial dye concentration of **10 mg L^{-1}** to evaluate the intrinsic catalytic efficiency of the biosynthesized Fe_2O_3 nanoparticles under controlled laboratory conditions. However, textile effluents may contain higher dye concentrations (>100 mg L^{-1}), where degradation efficiency could decrease due to saturation of active catalytic sites and possible mass transfer limitations. Further studies at higher dye concentrations are therefore required to assess the practical applicability of the system.Figure 10 (a), (b), (c) indicates the degradation kinetics of Reactive Orange ME2RL in the presence of biosynthesized Fe_2O_3 were evaluated using a pseudo-first-order kinetic model. The kinetic analysis was performed by plotting $\ln(C_0/Ct)$ against reaction time, where C_0 represents the initial dye concentration and Ct represents the concentration at time t. A linear relationship was observed, indicating that the degradation process follows pseudo-first-order kinetics. The rate constant (k) was determined from the slope of the linear plot and was found to be **0.036 min^{-1}** with a correlation coefficient (R^2) of **0.915**, demonstrating a good fit of the experimental data to the pseudo-first-order model. The observed kinetics suggest that the degradation rate primarily depends on the dye concentration, while the catalyst concentration remains effectively constant during the reaction. This behavior is commonly observed in heterogeneous catalytic degradation systems where adsorption of dye molecules onto the nanoparticle surface precedes oxidative degradation.

3.4. Analysis of Degraded Dye Products

For analytical characterization of degradation ,Orange ME2RL dye solution prior to treatment was used as the control in UV–Vis, HPLC, and GC–MS analyses. This untreated dye served as the reference to compare spectral changes and identify degradation products after nanoparticle treatment.

3.4.1. FTIR of orange ME2RL degradation:

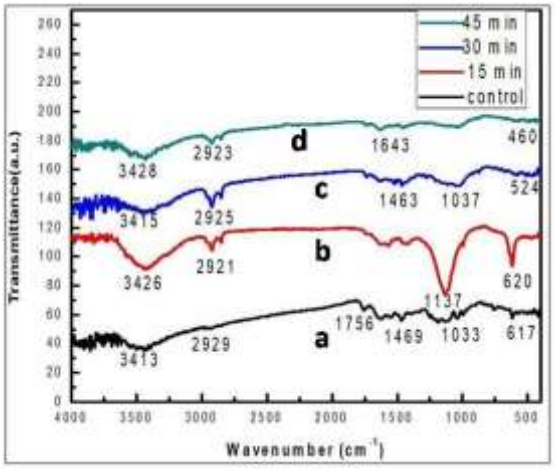

Fig. 11: FTIR of orange me2RL dye upon degradation - a) pure dye b) after 15 min c) after 30 min d) after 45 min

As shown in Figure 11, the broad band observed around 3410–3430 cm^{-1} corresponds to –OH/–NH stretching vibrations, indicating hydroxylated intermediates formed during dye degradation (Silverstein et al., 2014). The peaks near 2920–2930 cm^{-1} are attributed to aromatic or aliphatic C–H stretching vibrations (Stuart, 2004). The gradual reduction and eventual disappearance of the azo (–N=N–) bond vibration confirms cleavage of the dye chromophore, a key indicator of azo dye degradation (Saratale et al., 2011; Forgacs et al., 2004). The weakening of S=O and C–N stretching bands in the 1200–1000 cm^{-1} region (Figure 4.31) further supports the breakdown of sulfonated dye structures. The emergence of new low-frequency peaks (<700 cm^{-1}) suggests formation of low-molecular-weight inorganic or mineralized products after prolonged degradation (Roy et al., 2022).

3.4.2. HPLC Analysis

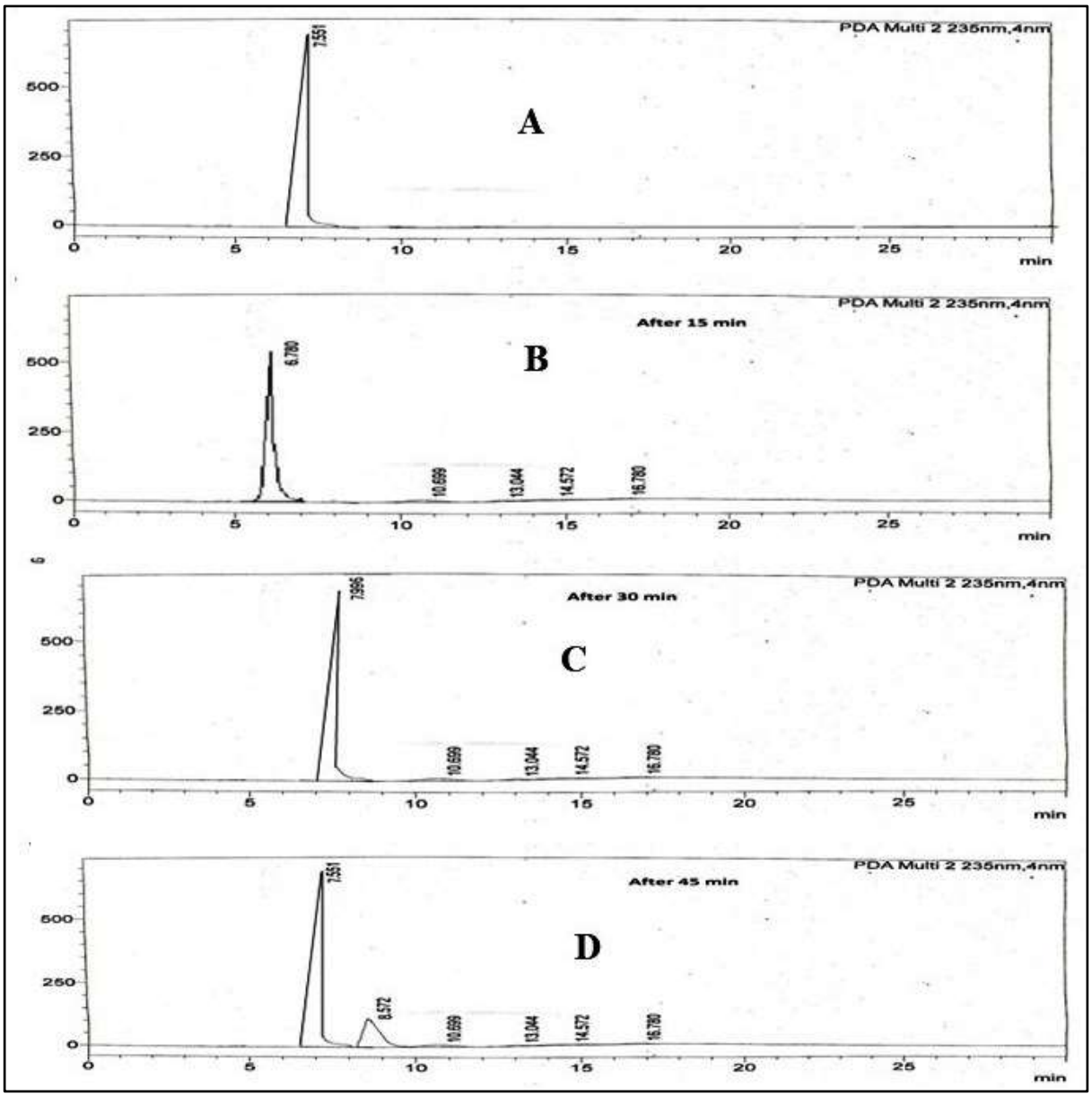

Fig. 12: HPLC chromatogram of reactive orange me2RL upon degradation – A) pure dye, B) after 15 min, C) after 30 min, D) after 45 min

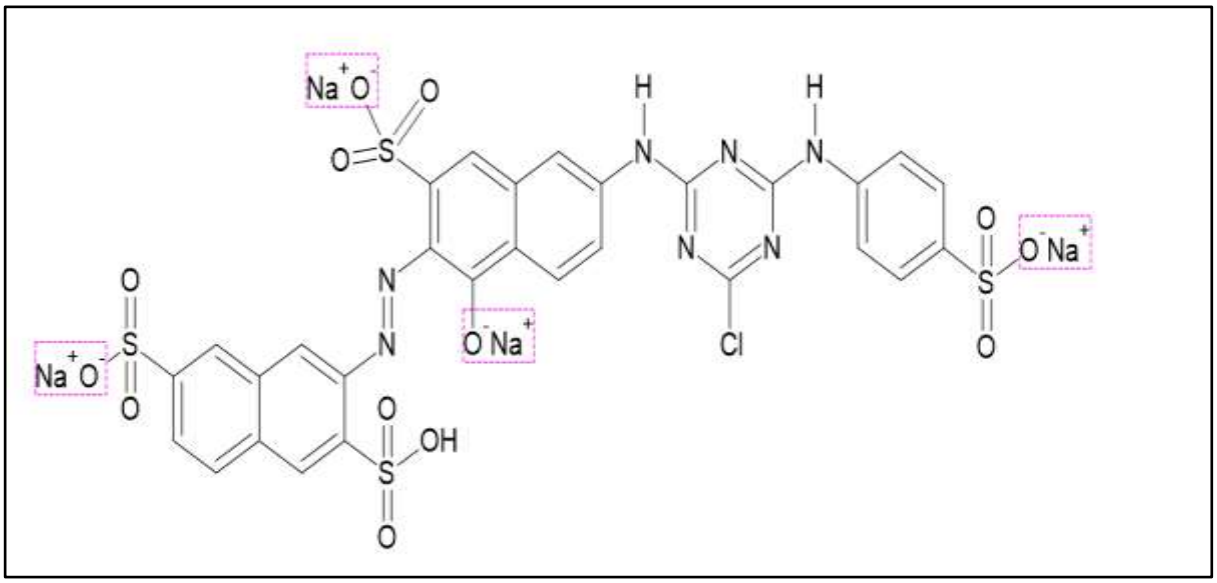

Fig. 13:Structure of dye Reactive Orange me2RL

The HPLC chromatogram of Reactive Orange Me2RL showed distinct retention peaks. After degradation, the standard peak disappeared and new peaks appeared at retention times of 8.572, 10.699, 13.044, 14.572, 4.017, and 16.780 minutes, confirming catalytic degradation of the dye (Gottlieb 2003) (Fig. 10, Fig. 11, Fig. 12).

3.4.3. GC–MS Analysis

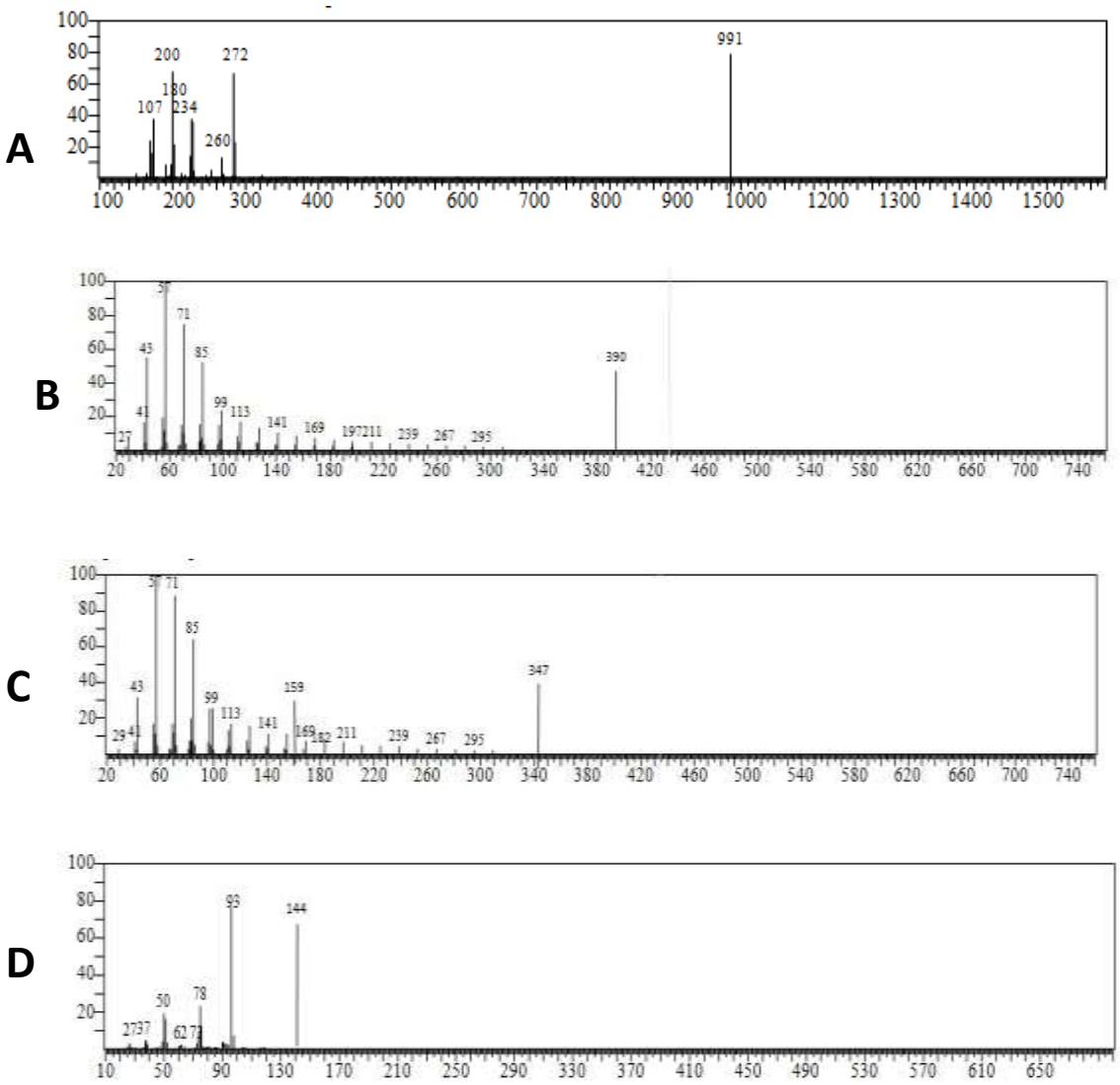

Fig. 14: GC-MS analysis of Reactive Orange me2RL: A) Control dye (Beforedegradation), B) Degradation after 15 min, C) Degradation after 30 min, D)Degradation after 45 min.

Degradation of Orange ME2RL dye was carried out using Fe_2O_3nanoparticles. This reaction yielded eight distinct compounds. The mass spectra of the control Orange ME2RL dye and its degraded metabolites, collected at intervals of 15 minutes as are presented in Fig. 14 (a), (b), and (c) (d) to illustrate the biodegradation pathway. During catalytic degradation, the aromatic ring of Orange ME2RL dye was cleaved, resulting in the formation of several metabolites, including Sodium 6-amino-5-sulfonatonapthalen-1yl-sulfite (1), Sodium 3-amino-7-[(4-chloro-1,3,5-triazin-2-yl)amino)-4 hydroxynapthalene-2-sulphonate (2), Sodium 4-aminobenzene-1-sulphonate (3), Naphthalen-2-amine (4), 2-aminonapthalen-1-ol (5), Aniline (6), Naphthalene-1-ol (7), and Benzene (8). GC-MS analysis demonstrates that biosynthesized Fe_2O_3nanoparticles acts as an effective catalyst, facilitating the degradation of Orange ME2RL into low molecular weight compounds.The metabolites detected by GC–MS were tentatively

identified by comparing the obtained mass spectra with the NIST mass spectral library. The proposed degradation pathway was constructed based on these intermediates and previously reported azo dye degradation mechanisms.

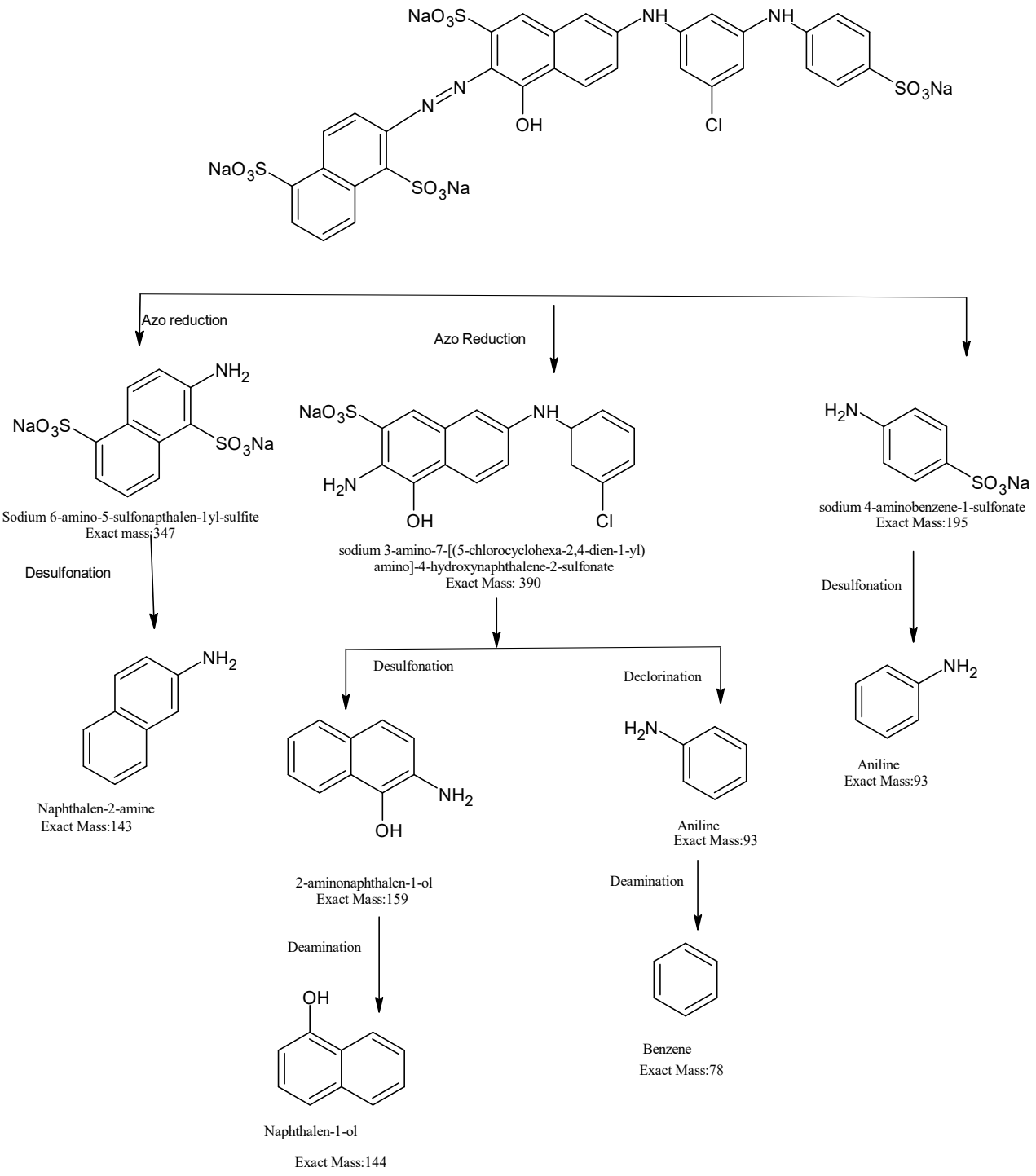

Fig. 15: Proposed degradation pathway of Reactive Orange M2RL dye based on GC MS analysis

.

3.5. Proposed Degradation Mechanism

The degradation of Reactive Orange M2RL by *Pseudomonas stutzeri*–mediated Fe_2O_3 nanoparticles proceeds via an adsorption–oxidation mechanism differs from the pathway proposed by Castro et al. (2020) for Orange ME2RL. Formation of intermediate ions analogous to m/z 347, 390, and 159 confirmed sequential azo bond scission, aromatic ring opening, and oxidative mineralization.

3.6. Antibacterial Activity

Antibacterial activity of iron nanoparticles was studied against pathogenic bacteria. Zones of inhibition were recorded. Outcomes in Fig. 15 and Table 1 indicate that FeNPs exhibited significant antimicrobial activity against *S. aureus* NCIM-2654 (25 mm), *S. typhi* NCIM-2501 (20 mm), *P. vulgaris* NCIM-2813 (16.33 mm), and *P. aeruginosa* NCIM-5032 (16.33 mm).Zone of inhibition measurements reported as mean ± standard deviation based on triplicate experiments**.**

Table 1:Antibacterial activity in terms of zone of inhibition (mm) in presence of nanoparticles and standard antibiotics

Test organism	**Diameter of zone of inhibition (mm) Nanoparticles**	**Std antibiotic**	**Std antibiotic + nanoparticles**
Staphylococcus aureus	25 ± 1	27 ± 0.57	28 ± 0.57
Pseudomonas aeruginosa	11.66 ± 0.57	20.33 ± 0.57	24.66 ± 0.57
Proteus vulgaris	15 ± 2.64	21 ± 1	25.66 ± 0.57
Salmonella typhi	20.66 ± 0.57	24.66 ± 0.57	26.33 ± 1.15

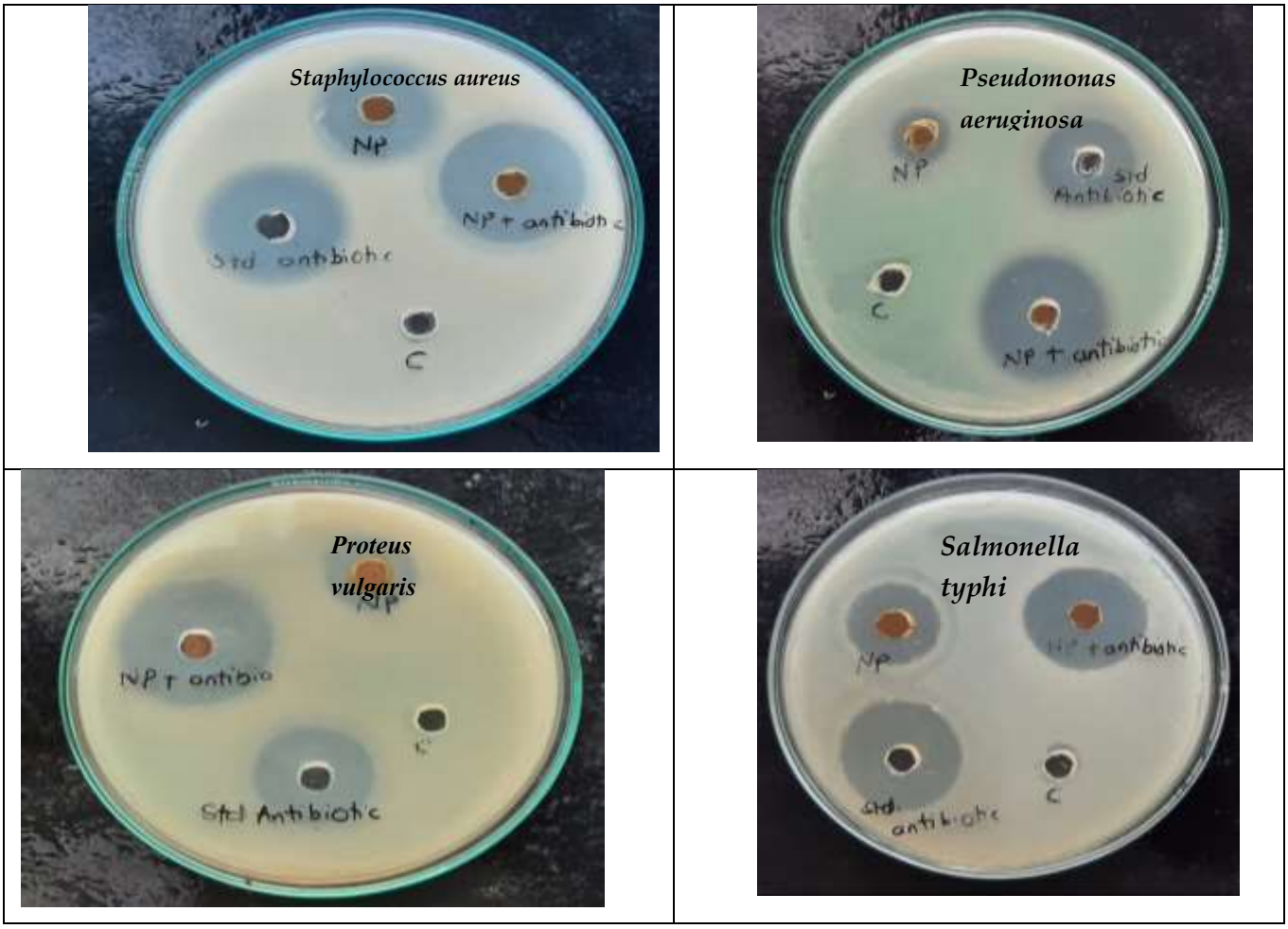

Fig. 16:Antibacterial activity of iron nanoparticles against *S. aureus* NCIM-2654, *P. aeruginosa* NCIM-5032, *P. vulgaris* NCIM-2813, and *S. typhi* NCIM-2501

Additionally, a combination of Fe NPs with antibiotic cefuroxime was tested, resulting in zones of inhibition of 28 mm for *S. aureus* NCIM-2654, 27 mm for *S. typhi* NCIM-2501, 26 mm for *P. vulgaris* NCIM-2813, and 25 mm for *P. aeruginosa* NCIM-5032.(Fig 16). This combination demonstrated enhanced antimicrobial activity, with increases of 0.15, 0.16, 0.39, and 0.56 fold, respectively. The antibacterial activity of Gram-negative as well as Gram-positive bacteria varied due to their distinct cell wall compositions (Zambare, Survase&Kanase 2023).The antibacterial activity of biosynthesized iron nanoparticles (Fe NPs) operates through multiple complementary mechanisms that effectively damage both Gram-positive and Gram-negative bacteria. Fe NPs first attach to the negatively charged bacterial cell surface, disrupting membrane integrity and increasing permeability. This facilitates nanoparticle entry into the cell, where the release of Fe^{2+} and Fe^{3+} ions triggers Fenton-like reactions, generating reactive oxygen species (ROS) such as hydroxyl and superoxide radicals. These ROS induce severe oxidative stress, damaging essential cellular components including lipids, proteins, and DNA, ultimately leading to membrane leakage, enzyme deactivation, and genetic material fragmentation. In Gram-negative bacteria, Fe NPs penetrate the outer membrane and periplasmic space, while in Gram-positive bacteria, the thick peptidoglycan layer traps nanoparticles, enabling sustained ROS production. When combined with cefuroxime, Fe NPs enhance

antibiotic effectiveness by weakening cell membranes, promoting antibiotic penetration, and reducing bacterial resistance by impairing efflux pumps and enzymes linked to β-lactam tolerance. Overall, Fe_2O_3 NPs exert antibacterial action through cell surface disruption, ROS-mediated damage, metal ion interference with metabolism, and antibiotic potentiation, demonstrating strong potential for managing multidrug-resistant bacterial pathogens (Hosseinzadeh 2025).Rather than synergistic effect, Fe_2O_3 nanoparticles along with standard antibiotics shows enhanced antibacterial affect.

3.7. Phytotoxicity

Seeds germinated in degradation products showed significant differences compared to those germinated in Orange me2RL, with a significance level of ($P < 0.05$), as resolved by Tukey–Kramer multiple comparison test. The degradation of dyes may not always yield benign byproducts; evidence suggests that it can potentially produce more harmful compounds. Studies conducted by the Gottlieb group revealed that treating azo dyes could result in the creation of aromatic amines that are even further toxic than the original dyes (Gottlieb et al. 2003). Consequently, a phytotoxicity assessment was undertaken to gauge the potential harm of degraded metabolite products on various plant seeds, such as Green gram, *Triticum aestivum*, *Vigna unguiculata* and *Pisum sativum*. All seeds were exposed to Reactive Orange me2RL dye and its degraded metabolites at a concentration of 100 ppm.

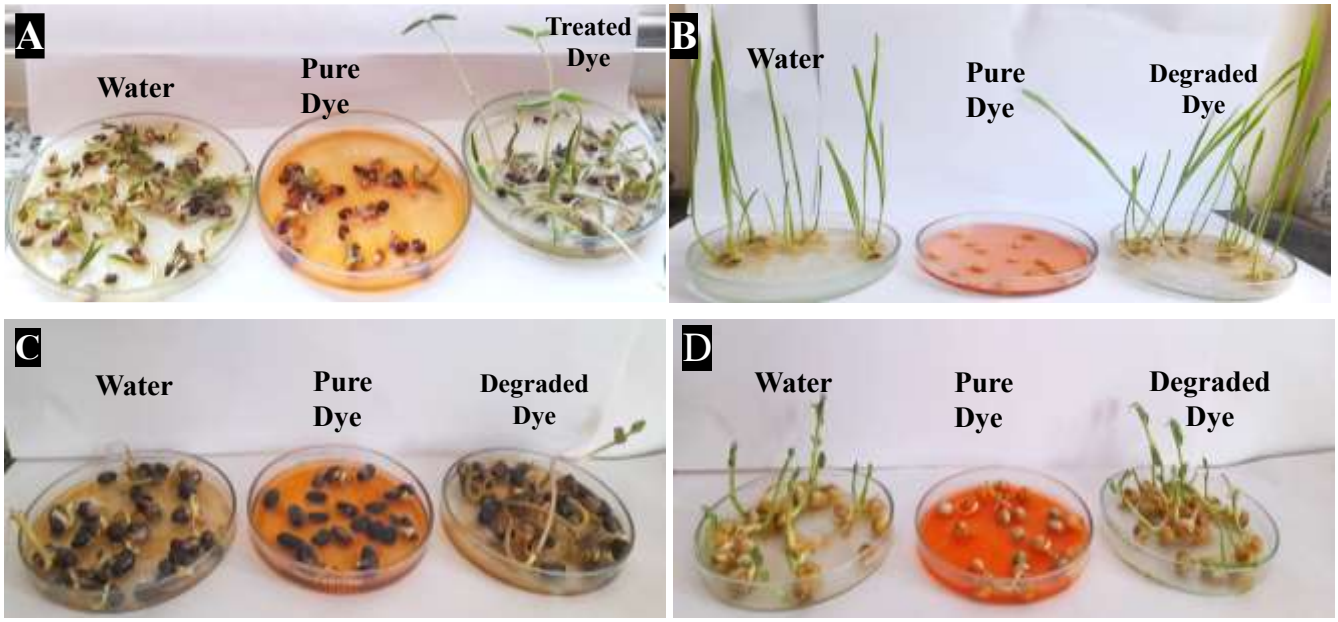

Fig. 17:Phytotoxicity analysis of pure dye reactive orange ME2RL and its metabolites using seed- A: Green gram, B. *Triticum aestivum*, C.*Vigna unguiculata* and D.*Pisum sativum*

The findings, outlined in Table 2 and Fig. 17, showed the germination rate as well as the lengths of radicles and plumules across all plant species tested. The degraded metabolites demonstrated a notable increase in both root and shoot lengths across all plant species. On the other hand, when compared to the degraded products, the untreated dye resulted in significantly lower seed germination rates and stunted shoot and root growth for all four plants.

Based on these results, it seems that the degradation products did more than just remove the toxicity; they also promoted seed growth (Survase&Kanase 2022). The improved growth parameters observed in *Vigna radiata* treated with degraded dye metabolites compared to the water control may indicate not only detoxification but also possible nutrient enrichment effects. During the degradation process, complex dye molecules are broken down into smaller organic intermediates and inorganic ions, which may act as additional nutrient sources for plant growth. These metabolites can enhance seed germination and seedling development by providing readily available carbon or nitrogen sources.

Table 2: Phytotoxicity analysis of pure dye reactive orange me2RL and its metabolites using seed Green gram, *Triticum aestivum*, *Vigna unguiculata* and *Pisum sativum*.

Parameters studied	**Water**	**Orange Me2RL**	**Degraded metabolites**
Vigna radiata			
Radial (cm)	2.1 ± 0.1	1.16 ± 0.057	2.5 ± 0.1
plumule(cm)	4.13 ± 0.11	0.23 ± 0.1	10.33 ± 0.57
Germination (%)	100	28.33 ± 2.88	100
Triticum aestivum			
Radial (cm)	1.86 ± 0.057	0.16 ± 0.057	3.1 ± 0.1
plumule(cm)	9.1 ± 0.1	0.23 ± 0.057	12.1 ± 0.1
Germination (%)	100	5	100
Vigna unguiculata			
Radial (cm)	14.1 ± 0.1	0.13 ± 0.057	8.03 ± 0.20
plumule(cm)	12.1 ± 0.1	0.26 ± 0.057	10.5 ± 0.1
Germination (%)	100	20	100
Pisum sativum			
Radial (cm)	3.9 ± 0.1	0.13 ± 0.057	3.76 ± 0.05
plumule(cm)	4.46 ± 0.057	2.5 ± 0.1	4.86 ± 0.05

Germination (%)	100	30	100

3.8. Fish Toxicity

To determine the lethal concentration of pure dye, fish were exposed to different concentrations of pure dye for 24, 48, 72, and 96 h. The percent mortality for pure dye at 96 h was calculated.

Table 3 : Effect of Orange ME2RL on mortality of *Cirrhinusmrigala* for 96 hrs exposure period.

No. of fishes	Concentration (ppm)	Exposure period (hrs.)				% mortality
		24	48	72	96	
10	1.25	0	0	0	0	0
10	2.50	0	0	0	1	10
10	3.75	0	0	1	2	30
10	**5.00**	**0**	**1**	**2**	**2**	**50**
10	6.25	1	1	2	3	70
10	7.5	1	2	3	3	90
10	8.75	6	4	-	-	100

The acute toxicity test showed that mortality of fish increased with increasing concentration of the test sample. No mortality was observed at 1.25 ppm after 96 h exposure, whereas complete mortality (100%) occurred at 8.75 ppm. Approximately 50% mortality was observed at 5 ppm, indicating that the 96 h LC_{50} value lies near this concentration.

The observed LC_{50} value was determined to be 5 ppm (5 µL/L)**,** while the statistically calculated LC_{50} value obtained from probit analysis was 4.8 ppm (≈4.5 µL/L)**.** The close agreement between the observed and calculated LC_{50} values indicates good consistency and reliability of the experimental data. This result suggests that the test compound exhibits significant toxic effects on fish even at relatively low concentrations.

3.8.1. Histological Observations of Liver

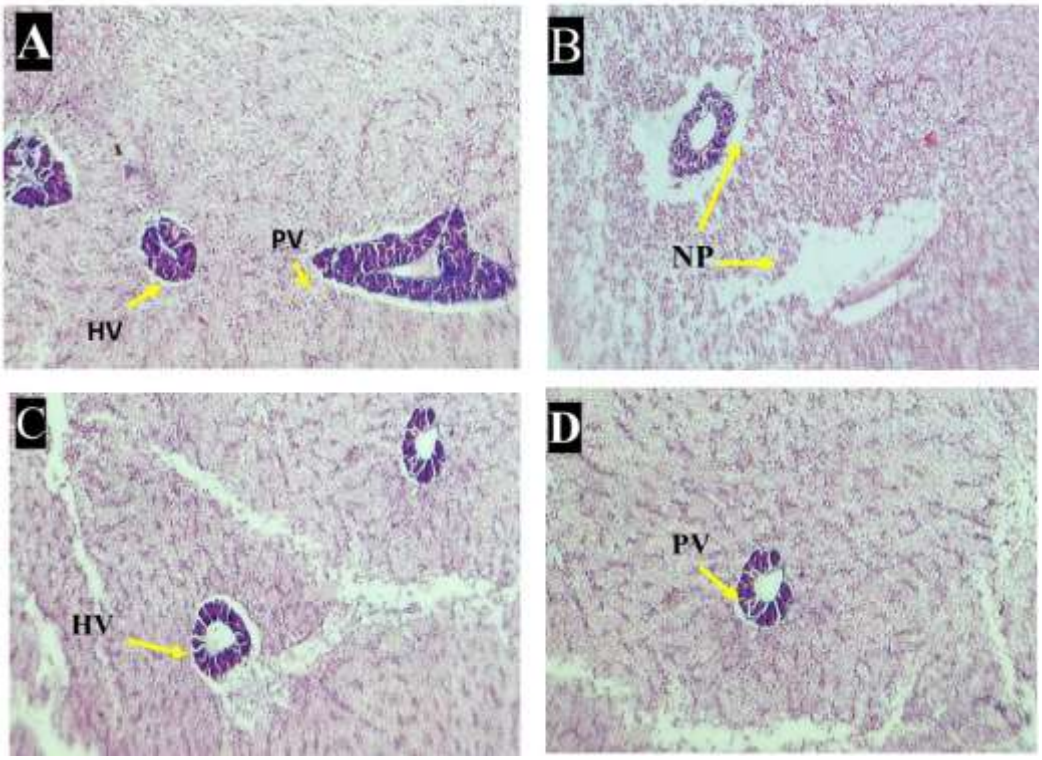

Fig. 18:Histopathological changes in liver: A: when grown in fresh water, B: exposure to pure dye, C: exposure to treated dye, D: exposure to nanoparticles

The histological structure of the liver of control fish is shown in the photomicrograph in Fig. 18. These photomicrographs of H-E-stainedphotomicrographs of liver slices stained with H-E revealed hepatic cells inside the bile canaliculi network. Hepatic cells had a spherical, blue-coloured nucleus positioned in the centre of a round to polygonal morphology. Glycogen granules were abundant in these cells. Hepatic cell cords, which are cord-like structures formed by hepatic cells encircling sinusoids, were not separate. Each of these cables had a centrally placed bile canaliculus visible. Hepatocytes were oriented with their bases facing the sinusoids and their apices facing the bile canaliculi wall. The arrangement of blood vessels and the bile duct was uneven, and there was no noticeable division of the hepatic cells within the lobules. Lipid droplets were seen inside rounded or elongated Ito cells, often known as fat-storing cells. Kupffer cells were seen occasionally lining the sinusoids with a substantial quantity of cytoplasm.The portal vein is observed, encased by pancreatic acini collectively referred to as the hepatopancreas. The hepatic arteries displayed a narrow lumen shielded by a dense layer of endothelial cells. Within every hepatic lobule, an intralobular central vein was noticeable, containing blood cells within its lumen.

The liver is a prime target for toxicants because of its extensive blood supply. In addition, several toxicants have been examined for their harmful effects on the liver since it is believed to be the principal organ for bioaccumulation (van Dyk, Pieterse& van Vuren 2007). When fish were subjected to a pure dye, notable degenerative alterations were observed in their livers compared to the control group (refer to Fig. 18). These histological changes were marked by significant disorganization of hepatic cords, widespread dilation of sinusoids throughout the tissue, and increased sinusoidal spaces surrounding the portal vein. Additionally, there was complete degeneration of hepatocytes with severe necrotic patches. Degeneration of cytoplasm, vacuolation within

hepatocytes, and evidence of karyolysis were also evident. Certain regions exhibited elongation of blood vessels, and the hepatopancreas underwent degeneration.

Fig. 18C and Fig. 18D depict the liver alterations induced by exposure to nanoparticles and the treated dye. Mild degenerative changes were noted in fish exposed to nanoparticles, even though less pronounced compared to the control group. These changes included hepatic cord disorganization, the onset of sinusoidal space expansion, cytoplasmic vacuolation, and cellular swelling, accompanied by pyknotic nuclei in some cells. Although degeneration was observed to a lesser extent, there were no significant alterations observed in the livers of fish exposed to nanoparticles compared to those exposed to pure dye.

3.8.2. Histological Observations of Gills

The histological structure of the gills of *Cerenus mrigala* closely resembles that of most freshwater teleosts. Each gill is covered by an operculum, with four pairs of gills present. These gills are supported by curved gill arches made of bony material and covered with multilayered epithelium. Each gill arch features two rows of gill filaments, known as primary gill lamellae, on one side only.These primary gill lamellae are wider at the base and taper towards the tip. They consist of a central vascular layer surrounded by a wall composed of three to four layers of epithelium, with a layer of connective tissue in between. The primary gill lamellae are supported by a central cartilaginous matrix covering the chondrocytes. The multilayered epithelium at the tip of primary gill lamellae consists mainly of oval to flat epithelial cells, with centrally located nuclei and homogenous, basophilic cytoplasm.

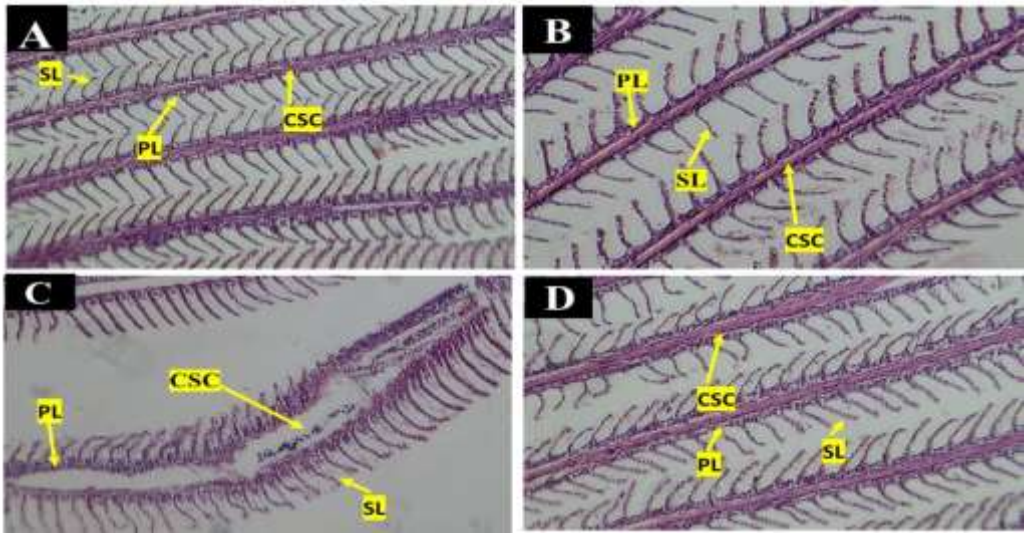

Fig. 19:Histopathological changes in gill- A: when grown in fresh water, B:exposure to pure dye, C: exposure to treated dye, D: exposure to nanoparticles

Additionally, each primary gill lamella possesses two rows of thin filamentous structures known as secondary gill lamellae or secondary gill filaments (Fig. 19 A), arranged perpendicular to the axis of the primary gill lamellae. The secondary gill lamellae appear to develop as outfoldings from primary gill lamellae. They consist of a single layer of epithelial cells, which are oval to cuboidal in shape with basophilic cytoplasm and centrally placed oval nuclei. Internally, the secondary lamellae contain a central core composed of blood sinuses lined and spanned by large oval to rounded pillar cells. These pillar cells have homogenous, basophilic cytoplasm and centrally located round nuclei.

Following 96 h of exposure to pure dye, degenerative alterations were noted in the gill structure. Tilting and congestion were observed at the tips of the primary gill lamellae (refer to Fig. 19C). Additionally, detachment of the epithelium from the central supporting material of the primary gill lamellae was evident. Significant enlargement of the central supporting material of the primary gill lamellae was also observed.Furthermore, progressive hyperplasia and thickening of the epithelium at the interlamellar region were observed. Shortening and fusion of adjacent secondary gill lamellae were noted in a certain region, as shown in Fig. 19C.

Mild histopathological changes were observed in the gills following exposure to degraded dye, as depicted in Fig. 19 B. A slight enlargement of the tips of the primary gill lamellae was noted,with these dilated tips being filled with blood cells. An increased number of mucous cells, particularly at the tips of the primary gill lamellae, was also observed (refer to Fig. 19 B). Additionally, the secondary gill lamellae appeared curved with dilated tips filled with blood cells.There was a slight desquamation of the lining of epithelial cells from the central supporting cartilage when exposed to nanoparticles (Fig. 19D). These alterations were not as significant as those observed following exposure to pure dye.

4. Conclusions

This study presents the eco-friendly biosynthesis of Fe_3O_4 nanoparticles using *Pseudomonas stutzeri.* Characterization by UV–visible spectroscopy, SEM, FTIR, XRD, HRTEM, and DLS confirmed predominantly spherical particles sized 30–50 nm. The nanoparticles demonstrated strong catalytic activity in degrading Reactive Orange ME2RL dye, with degradation metabolites identified by FTIR, HPLC, and GC–MS. They also showed antibacterial activity against *Staphylococcus aureus, Salmonella typhi, Proteus vulgaris,* and *Pseudomonas aeruginosa*, with greater inhibition when combined with antibiotics. Phytotoxicity and fish toxicity tests revealed reduced toxicity of the degraded dye products compared to the original dye. The synthesized Fe_2O_3 nanoparticles showed high degradation efficiency toward the dye, indicating their suitability for treatment of dye-containing industrial effluents Fe_2O_3 nanoparticles possess inherent magnetic properties that enable easy separation and possible reuse of the catalyst from treated wastewater using an external magnetic field. Therefore, this study provides a sustainable and efficient approach for the remediation of textile dye pollutants and has potential applicability in large-scale industrial wastewater treatment processes.Further studies are required to evaluate the reusability and long-term stability of the synthesized Fe_2O_3 nanoparticles over multiple degradation cycles to assess their practical applicability in wastewater treatment. Due to the magnetic nature of Fe_2O_3 nanoparticles, recovery and reuse may be feasible, which will be explored in future studies.

Acknowledgments:

The authors are grateful to the Rayat Institute of Research and Development, Satara, for providing the prestigious Dr. B.M. Sawant fellowship and laboratory facilities as financial provision for the research endeavour.

CRediT authorship contribution statement

Pradnya Zambare: Writing – original draft, Data curation, Conceptualization, Visualization, Validation, Methodology, Investigation, Formal analysis. **AvinashRaut:** editing, Investigation, Formal analysis. **ShivangiKanase:** Conceptualization, Project administration, Supervision, Funding acquisition, Writing – review & editing.

Conflicts of Interest: The authors declare that there is no conflict of interest with this research

5. REFERENCES

1. Acharya, C., Mishra, S., Chaurasia, S.K., Pandey, B.K., Dhar, R. and Pandey, J.K., 2025. Synthesis of metallic nanoparticles using biometabolites: mechanisms and applications. *In: BioMetals*, Vol. 38(1). Springer: Cham, Switzerland, pp. 21–54.
2. Ali, H. Biodegradation of Synthetic Dyes,A Review. Water, Air, Soil Pollut.2010, 213, 251−273.
3. Al-Musawi, T.J., McKay, G., Rajiv, P., Mengelizadeh, N. and Balarak, D., 2022. Sonophotocatalytic degradation of Acid Blue 113 using $CoFe_2O_4$-MWCNT nanocomposite. *In: Journal of Photochemistry and Photobiology A: Chemistry*, Vol. 424. Elsevier: Amsterdam, Netherlands, p. 113617.
4. Ameur, W.B., de Lapuente, J., El Megdiche, Y., Barhoumi, B., Trabelsi, S., Camps, L. and Borràs, M., 2012. Oxidative stress, genotoxicity and histological effects in fish from Bizerte Lagoon. *In: Marine Pollution Bulletin*, Vol. 64(2). Elsevier: Amsterdam, Netherlands, pp. 241–251.
5. Apine, O., Patil, S., Patil, D. and Jadhav, J.P., 2023. Role of analytical techniques in treatment of synthetic dyes and textile effluent. *In: Pandey, A. et al. (eds) Current Developments in Bioengineering and Biotechnology*. Elsevier: Amsterdam, Netherlands, pp. 303–338.
6. Banat, I.M., Nigam, P., Singh, D. and Marchant, R., 1997. Microbial decolorization of textile-dye-containing effluents: a review. *In: Bioresource Technology*, Vol. 61(1). Elsevier: Amsterdam, Netherlands, pp. 103–115.
7. Bhattacharjee, S. (2016). DLS and zeta potential–what they are and what they are not?. *Journal of controlled release*, *235*, 337-351.
8. Castro, L., Meurer, E., Alves, H., Santos, M., Vasques, E. and Colpini, L., 2020. Photocatalytic degradation of Orange-122 via electrospray MS. *In: Brazilian Archives of Biology and Technology*, Vol. 63. SciELO: São Paulo, Brazil, p. e20180573.

9. Chavan, R.B., 2001. Indian textile industry—environmental issues. *In: Indian Journal of Fibre and Textile Research*, Vol. 26(1–2). CSIR: New Delhi, India, pp. 11–21.

10. Chicea, D., Indrea, E. and Cretu, C.M., 2012. Assessing Fe_3O_4 nanoparticle size by DLS, XRD and AFM. *In: Journal of Optoelectronics and Advanced Materials*, Vol. 14(5). Romania, pp. 460–466.

11. Ferreira, F.N., Benevides, A.P., Cesar, D.V., Luna, A.S. and de Gois, J.S., 2020. Magnetic solid-phase extraction of estrogenic compounds using maghemite–graphene oxide nanoparticles. *In: Microchemical Journal*, Vol. 157. Elsevier: Amsterdam, Netherlands, p. 104947.

12. Forgacs, E., Cserháti, T. and Oros, G., 2004. Removal of synthetic dyes from wastewaters: a review. *In: Environment International*, Vol. 30(7). Elsevier: Amsterdam, Netherlands, pp. 953–971.

13. Giuli, G., Trapananti, A., Mueller, F., Bresser, D., d'Acapito, F. and Passerini, S., 2015. Effects of Fe and Co doping on nanosized ZnO structure. *In: Inorganic Chemistry*, Vol. 54(19). ACS: Washington DC, USA, pp. 9393–9400.

14. Gottlieb, A.L., 2003. Microbial degradation of textile dyes to safe end-products. *In: Doctoral Thesis*. Nottingham Trent University: Nottingham, UK, pp. 1–180.

15. Gottlieb, A., Shaw, C., Smith, A., Wheatley, A. and Forsythe, S., 2003. Toxicity of textile azo dyes after hydrolysis and decolourization. *In: Journal of Biotechnology*, Vol. 101. Elsevier: Amsterdam, Netherlands, pp. 49–56.

16. Gupta, V. K.; Mittal, A.; Gajbe, V.; Mittal, J. Removal and recovery of the hazardous azo dye acid orange 7 through adsorption over waste materials: bottom ash and de-oiled soya. Ind. Eng. Chem. Res. 2006, 45, 1446−1453

17. Haroon, K., Kherb, J., Jeyaseelan, C. and Sen, M.J.N.E., 2023. Recent advances and sustainable approaches towards efficient wastewater treatment using natural waste derived nanocomposites: A review. Nature Environment & Pol-lution Technology, 22(3). 10.46488/NEPT.2023.v22i03.051

18. Holzwarth, U. and Gibson, N., 2011. The Scherrer equation versus the Debye–Scherrer equation. *In: Nature Nanotechnology*, Vol. 6(9). Nature Publishing Group: London, UK, pp. 534–535.

19. Hosseinzadeh, H., 2025. Antibacterial/magnetic iron oxide nanoparticles: synthesis, doping and applications. *In: Journal of Applied Material Science*, Vol. 1(3). Elsevier: Amsterdam, Netherlands, p. e210146.

20. Islam, M.A., Amin, S.N., Brown, C.L., Juraimi, A.S., Uddin, M.K. and Arshad, A., 2021. LC50 of pesticides and histopathology in African catfish. *In: Toxics*, Vol. 9(12). MDPI: Basel, Switzerland, p. 340.

21. Jana, J., Ganguly, M. and Pal, T., 2016. Surface plasmon resonance of metal nanoparticles for spectroscopic applications. *In: RSC Advances*, Vol. 6(89). Royal Society of Chemistry: London, United Kingdom, pp. 86174–86211.

22. Javidparvar, A.A., Ramezanzadeh, B. and Ghasemi, E., 2016. Effect of surface treatment of Fe_3O_4 nanoparticles on epoxy coating corrosion resistance. *In: Journal of the Taiwan Institute of Chemical Engineers*, Vol. 61. Elsevier: Amsterdam, Netherlands, pp. 356–366.

23. Joshi, A., Nanani, J., Trivedi, N., Kothari, V. and Kothari, R., 2015. Decolorization of Reactive Orange Me2RL by bacterial consortium. *In: National Science Symposium Proceedings*, Vol. 2. India, p. 164.

24. Joshi, A.U., Hinsu, A.T., Kotadiya, R.J., Rank, J.K., Andharia, K.N. and Kothari, R.K., 2020. Decolorization and biodegradation of textile di-azo dye Acid Blue 113 by *Pseudomonas stutzeri* AK6. *In: 3 Biotech*, Vol. 10(5). Springer: Singapore, p. 214.

25. Katata-Seru, L., Moremedi, T., Aremu, O.S. and Bahadur, I., 2018. Green synthesis of iron nanoparticles using *Moringa oleifera* extracts. *In: Journal of Molecular Liquids*, Vol. 256. Elsevier: Amsterdam, Netherlands, pp. 296–304.

26. Khan, I., Saeed, K. and Khan, I., 2019. Nanoparticles: properties, applications and toxicities. *In: Arabian Journal of Chemistry*, Vol. 12(7). Elsevier: Amsterdam, Netherlands, pp. 908–931.

27. Mane, U.V., Gurav, P.N., Deshmukh, A.M. and Govindwar, S.P., 2008. Degradation of textile dye Reactive Blue 59 by *Streptomyces krainskii* SUK-5. *In: Malaysian Journal of Microbiology*, Vol. 4(2). Malaysia, pp. 1–5.

28. Mukherjee, B. and Dutta, S., 2019. Isolation of a phosphate-solubilizing bacterial strain *Bacillus tequilensis* MCC 3872 from rice field and characterization of its plant growth-promoting traits. *In: Pharma Innovation Journal*, Vol. 8. India, pp. 956–962.

29. Naz, M., Rafiq, A., Ikram, M., Haider, A., Ahmad, S.O., Haider, J. and Naz, S., 2021. Elimination of dyes by catalytic reduction in the absence of light: a review. *In: Journal of Materials Science*, Vol. 56(28). Springer: Berlin, Germany, pp. 15572–15608.

30. Nurbas, M.A., Ghorbanpoor, H.A. and Avci, H.Ü., 2017. Eco-friendly synthesis of magnetite (Fe_3O_4) nanoparticles using *Platanus orientalis* leaf extract. *In: Digest Journal of Nanomaterials and Biostructures*, Vol. 12(4). Romania, pp. 1231–1240.

31. Palleroni, N.J., 1984. *Pseudomonas*. *In: Krieg, N.R. (ed.) Bergey's Manual of Systematic Bacteriology*, Vol. I. Williams and Wilkins: Baltimore, United States, pp. 141–199.

32. Palleroni, N.J., Doudoroff, M., Stanier, R.Y., Solanes, R.E. and Mandel, M., 1970. Taxonomy of the aerobic pseudomonads: the properties of the *Pseudomonas stutzeri* group. *In: Microbiology*, Vol. 60(2). United Kingdom, pp. 215–231.

33. Palleroni, N.J., Kunisawa, R., Contopoulou, R. and Doudoroff, M., 1973. Nucleic acid homologies in the genus *Pseudomonas*. *In: International Journal of Systematic Bacteriology*, Vol. 23. United States, pp. 333–339.

34. Pandey, A., Singh, P. and Iyengar, L., 2007. Bacterial decolorization and degradation of azo dyes. *In: International Biodeterioration and Biodegradation*, Vol. 59(2). Elsevier: Amsterdam, Netherlands, pp. 73–84.

35. Patel, D.D. and Bhatt, S., 2022. Environmental pollution, toxicity profile, and physico-chemical and biotechnological approaches for treatment of textile wastewater. *In: Biotechnology and Genetic Engineering Reviews*, Vol. 38(1). Taylor & Francis: London, United Kingdom, pp. 33–86.

36. Periyasamy, A.P., 2024. Recent advances in the remediation of textile-dye-containing wastewater: prioritizing human health and sustainable wastewater treatment. *In: Sustainability*, Vol. 16(2). MDPI: Basel, Switzerland, p. 495.

37. Rossello, R., Garcia-Valdes, E., Lalucat, J. and Ursing, J., 1991. Genotypic and phenotypic diversity of *Pseudomonas stutzeri*. *In: Systematic and Applied Microbiology*, Vol. 14(2). Elsevier: Amsterdam, Netherlands, pp. 150–157.

38. Saha, S. and Bhunia, A.K., 2018. Synthesis of Fe_2O_3 nanoparticles and study of structural and optical properties. *In: Materials Today: Proceedings*. Elsevier: Amsterdam, Netherlands, pp. 1–8.

39. Sekar, S., Surianarayanan, M., Ranganathan, V., MacFarlane, D. and Mandal, A., 2012. Choline-based ionic liquids enhance biodegradation of azo dyes. *In: Environmental Science and Technology*, Vol. 46(9). ACS: Washington DC, United States, pp. 4902–4908.

40. Shahriarinour, M., Divsar, F., Dahka, F.K., Chegini, S.N., Mahani, M., Moeini, A. and Cerruti, P., 2021. Biodegradation of alprazolam in pharmaceutical wastewater using mesoporous nanoparticle-adhered *Pseudomonas stutzeri*. *In: Molecules*, Vol. 27(1). MDPI: Basel, Switzerland, p. 237.

41. Shakoor, S., Khan, M.S. and Khan, M.E., 2025. Adsorptive remediation of dyes through a novel approach from nano-technology: A comprehensive review. Nature Environment and Pollution Technology, 24(1), pp.1-15. 10.46488/NEPT.2025.v24i01.B4185

42. Srivastava, S.K. and Constanti, M., 2012. Room-temperature biogenic synthesis of multiple nanoparticles by *Pseudomonas aeruginosa* SM1. *In: Journal of Nanoparticle Research*, Vol. 14. Springer: Dordrecht, Netherlands, pp. 1–10.

43. Survase, A. and Kanase, S., 2022. Green synthesis of TiO_2 nanospheres by *Aspergillus eucalypticola* SLF1 and dye degradation. *In: Ceramics International*, Vol. 49(10). Elsevier: Amsterdam, Netherlands, pp. 14964–14980.

44. Van Dyk, J.C., Pieterse, G.M. and van Vuren, J.H.J., 2007. Histological changes in liver of *Oreochromis mossambicus* after cadmium and zinc exposure. *In: Ecotoxicology and Environmental Safety*, Vol. 66. Elsevier: Amsterdam, Netherlands, pp. 432–440.

45. Vasantharaj, S., Sathiyavimal, S., Senthilkumar, P., Lewis-Oscar, F. and Pugazhendhi, A., 2019. Biosynthesis of iron oxide nanoparticles using leaf extract of *Ruellia tuberosa*. *In: Journal of Photochemistry and Photobiology B: Biology*, Vol. 192. Elsevier: Amsterdam, Netherlands, pp. 74–82.

46. Velusamy, P., Kumar, G.V., Jeyanthi, V., Das, J. and Pachaiappan, R., 2016. Bio-inspired green nanoparticles: synthesis, mechanism and antibacterial application. *In: Toxicological Research*, Vol. 32. Korea, p. 95.

47. Wu, K., Shi, M., Pan, X., Zhang, J., Zhang, X., Shen, T. and Tian, Y., 2022. Decolorization and biodegradation of methylene blue dye by ligninolytic enzyme-producing *Bacillus thuringiensis*. *In: Enzyme and Microbial Technology*, Vol. 156. Elsevier: Amsterdam, Netherlands, p. 109999.

48. X.H. Vu, L.H. Phuoc, N.D. Dien, T.T.H. Pham, L.D. Thanh, Photocatalytic degrada tion of Methylene Blue (MB) over α-Fe2O3 nanospindles prepared by a hydro thermal route, J. Electron. Mater. 48 (2019) 2978–2985.

49. Y. Huang, D. Ding, M. Zhu, W. Meng, Y. Huang, F. Geng, J. Li, J. Lin, C. Tang, Z. Lei, Facile synthesis of α-Fe 2 O 3 nanodisk with superior photocatalytic performance and mechanism insight, Sci. Technol. Adv. Mater. 16 (2015) 014801.

50. Zambare, P., Survase, A. and Kanase, S., 2023. Green synthesis of copper nanoparticles using leaf extract of *Ocimum sanctum* and its antimicrobial activity. *In: International Journal of Pharmaceutical Investigation*, Vol. 13(1). India, pp. 106–112.

51. Zhao, H., Huang, M., Wu, J., Wang, L. and He, H., 2016. Preparation of Fe_3O_4@PPy magnetic nanoparticles for preconcentration of phthalates. *In: Journal of Chromatography B*, Vol. 1011. Elsevier: Amsterdam, Netherlands, pp. 33–44